Attenuation of gaseous detonations by porous media of fine microstructure

Miltiadis V. Papalexandris

Institute of Mechanics, Materials and Civil Engineering,
Université catholique de Louvain,
1348 Louvain-la-Neuve, Belgium

Abstract

This article reports on numerical simulations of detonation propagation in channels that contain one or more porous obstructions. The porous media considered herein have high porosity and are of fine microstructure, *i.e.* the diameter of the fibres of the solid matrix is smaller than the characteristic chemical length scale. Our study is based on a thermo-mechanical model for flows in superposed porous and pure-fluid regions. According to it, the solid matrix is represented as a rigid continuum and its porosity is introduced as a distribution that varies in space. With regard to chemical kinetics, two different three-step chain-branching schemes are considered; their difference being in the termination reaction. Our simulations predict that, even at high porosity, the porous obstructions act as a highly efficient momentum sink, thereby causing the detonation to attenuate significantly. In the case of a single porous section, the detonation re-initiates downstream via chain-branching explosion. However, arrays of porous zones that span the entire cross section of the domain produce a decoupling of the reaction zone from the leading shock, thereby effectively suppressing the detonation. Also, our study reveals that in domains with arrays of porous blocks that only partially cover the cross section of the channel, the detonations do not quench. Instead, they propagate as low-velocity detonations, the properties of which are elaborated herein as well.

Keywords: detonation simulation, porous media, chain-branching, detonation suppression, quasi-detonation, low-speed detonation, detonation

Email address: miltos@uclouvain.be (Miltiadis V. Papalexandris)

1. Introduction

A gaseous detonation that propagates in a tube or a channel can be attenuated via chemical or mechanical means. Chemical means involve the use of diluents or chemical inhibitors; see, for instance, [1–4]. The latter ones are compounds that participate in endothermic reactions with radicals. Mechanical means typically involve detonation diffraction into a much larger area or the use of solid obstacles. In the case of diffraction, the detonation attenuates via its interaction with the rarefaction that is formed as the reacting gas expands into the larger area [5–8]. On the other hand, in the case of solid obstacles, the main factor for detonation attenuation is the force exerted by the obstacles which acts as a sink of momentum and kinetic energy for the reactive mixture; see, for example, [9–12] and references therein.

Quite often, arrays of discrete, sparsely spaced solid obstacles fixed to the tube walls result in quasi-detonations. These are detonations that propagate at velocities significantly lower than those of the equivalent Chapman-Jouguet (CJ) detonations, *i.e.* they exhibit a velocity deficit. In the past, various researchers investigated the structure and propagation mechanism of quasi-detonations theoretically [13, 14], numerically [14, 15] or experimentally [10, 16–21]. These investigations established that quasi-detonations are sustained due to re-ignitions through shock reflections from the tube walls. However, it is not yet clear if the principal factor contributing to re-ignition is adiabatic compression by the reflected shocks or turbulent mixing.

On the other hand, ensembles of densely spaced obstacles can macroscopically be assimilated as a porous medium. The propagation characteristics of gaseous detonations through porous media have also been the topic of various research efforts in the past. Experimental studies have been presented, among others, in [9, 22–24]; see also the review article [25]. These studies confirmed the large amounts of momentum loss and the transition to quasi-detonation caused by porous obstacles. Further, they provided insight about the re-initiation mechanism of the detonation downstream of the porous medium.

More recently, experimental investigations have been presented in [26] on detonation suppression in rectangular channels with highly porous coatings on the walls. In this study, different equivalence ratios were considered, while the coatings were made of polyurethane foam (with porosity of 95 %) or steel

wool (with porosity of 99 % and average fibre size of 30 μm). It was reported that, in both cases, the detonation in the porous coating decouples into a shock and a subsonic flame. Subsequently, the same authors studied the effect of polyurethane coatings of different pore size on stoichiometric H_2/air mixtures [27, 28].

With regard to theoretical analyses and numerical simulations, in earlier models [9, 11, 14, 29–31] the presence of the porous medium was represented as a volumetric momentum sink whose amplitude is set by a constant friction factor. Such models, however, cannot accommodate spatially varying porosity and, therefore, cannot be used to study multi-dimensional flows. More recently, the authors of [32] presented detailed numerical simulations of detonation transmission through an array of solid cylindrical obstacles. In that study, the obstacles were represented in a discrete manner, which allowed the authors to elucidate the details of the flow structure in the region of the cylinders and the mechanism for detonation re-initiation downstream.

In all the aforementioned studies, the size of the micro-elements (spheres or fibres) comprising the solid matrix was comparable to or much larger than the length of the reaction zone. By contrast, the present paper is concerned with porous media whose fibres are considerably smaller than the reaction-zone length; for example, at the order of a micrometer. These are referred to herein as porous media of "fine microstructure". They can readily be produced by modern manufacturing technologies and can potentially be used in detonation arrestors or as means to modulate detonation behaviour. Nonetheless, to the author's knowledge, results for their effect on detonations are currently unavailable.

The present study consists of numerical simulations of unsteady flows via shock-capturing algorithms. Due to the small size of the fibres of the solid matrix, the porous obstacles are modelled as rigid solid continua and their porosity is introduced as a field variable that is constant in time but varies in space. With regard to chemical kinetics, two different three-step chain branching mechanisms are considered. Their difference lies on the termination reaction; one is suitable at high- and the other one at lower-pressure conditions. The paper is organized as follows. In Section 2, we present the governing equations and outline their basic characteristics. Also, we elaborate on the chemical kinetics mechanisms employed in our study. In Section 3, we first outline the set up of the numerical simulations and subsequently present and analyze the numerical results. Finally, Section 4 concludes.

2. Mathematical model

In the numerical study presented herein we employ the mathematical model of [33] for flows in superposed porous and pure-fluid regions. This model is based on the same formalism and principles as the two-phase continuum theory of [34] for fluid-solid mixtures. According to it, the fluid and solid phases are treated as separate continuous thermodynamic systems. However, in the case of the model in [33], the matrix (or skeleton) of the porous material is assumed to be a rigid solid of zero velocity and constant mass density. Also, in the present work, the solid matrix is assumed to be chemically inert and not subject to phase change.

As is typical in two-phase continuum theories, the porosity $\phi(\boldsymbol{x})$ is introduced as a concentration parameter (or distribution) that measures the density of volume occupied by the fluid. In other words, the porosity is a field variable that remains constant in time and is defined by,

$$\phi(\boldsymbol{x}) \;=\; \frac{\mathrm{d}V_{\mathrm{f}}}{\mathrm{d}V}\,, \tag{1}$$

where V_{f} is the volume occupied by the fluid and V is the volume of the physical space. For the purposes of our study, we assume that $\phi(\boldsymbol{x})$ is a continuous function. Consequently, macroscopic interfaces of porous and pure-fluid regions are not sharp but are assumed to be smooth, *i.e.* they have a finite thickness. This implies that the number density of the fibres that constitute the solid matrix does not jump from a finite value to zero but, instead, decreases continuously to zero. It should be noted that the presumed smoothness of the interfaces does not pose any modeling or numerical issues because the interface thickness can be assumed to be as small as desired.

The gaseous reactive mixture is considered to consist of three major species: reactants F, radicals R and combustion products P. Further, we assume negligible heat diffusion and viscous dissipation for the gas. Accordingly, the mass, momentum and energy balance laws for the gaseous phase read, in dimensionless form,

$$\frac{\partial}{\partial t}(\phi\rho) + \nabla\cdot(\phi\rho\boldsymbol{u}) \;=\; 0\,, \tag{2}$$

$$\frac{\partial}{\partial t}(\phi\rho\boldsymbol{u}) + \nabla\cdot(\phi\rho\boldsymbol{u}\boldsymbol{u}) + \nabla(\phi p) \;=\; \boldsymbol{f}\,, \tag{3}$$

$$\frac{\partial}{\partial t}(\phi\rho e_{\mathrm{t}}) + \nabla\cdot(\phi(\rho e_{\mathrm{t}} + p)\boldsymbol{u}) \;=\; \boldsymbol{f}\cdot\boldsymbol{u} + \mathcal{E}\,, \tag{4}$$

where e_t stands for total energy of the gas, $\boldsymbol{f}$ for the momentum exchange between the two phases and $\mathcal{E}$ for the interphasial heat exchange. According to [33], the constitutive expressions for $\boldsymbol{f}$ and $\mathcal{E}$ are, respectively,

$$\boldsymbol{f} \;=\; p\nabla\phi - \boldsymbol{\beta}\cdot\boldsymbol{u}\,, \tag{5}$$

and

$$\mathcal{E} \;=\; h(T - T_\mathrm{s})\,, \tag{6}$$

where $\boldsymbol{\beta}$ is the matrix of interphasial drag parameters, T and T_s are the temperatures of the gas and solid matrix respectively, and h is the interphasial heat-exchange coefficient. For orthotropic porous media, $\boldsymbol{\beta}$ is diagonal. Orthotropic media are those whose material properties at any point differ along three mutually orthogonal axes with each axis having twofold rotational symmetry. On the other hand, for isotropic porous media, *i.e.*, media whose mechanical properties at any point are identical in all directions, $\boldsymbol{\beta}$ is diagonal with identical diagonal elements.

Also, the species concentration laws read,

$$\frac{\partial}{\partial t}(\phi\rho Y_j) + \nabla\cdot(\phi\rho\boldsymbol{u}Y_j) \;=\; \dot{\omega}_j\,, \qquad j = \mathrm{F},\,\mathrm{R},\,\mathrm{P}\,, \tag{7}$$

where Y_j stands for the mass fraction of the species j and $\dot{\omega}_j$ for the source term due to the chemical reactions in which this species participates. Since $Y_\mathrm{F} + Y_\mathrm{R} + Y_\mathrm{P} = 1$, then only two of the equations (7) have to be solved for. For simplicity purposes, we assume that F, R and P are perfect gases with equal heat-capacity ratio γ. As such, the thermal equation of state of the mixture reads, in dimensionless form, $p = \rho T$. Then, the total energy of the gaseous phase can be written as,

$$e_\mathrm{t} \;=\; \frac{1}{\gamma-1}\frac{p}{\rho} + \frac{1}{2}\boldsymbol{u}\cdot\boldsymbol{u} + q\,(Y_\mathrm{F} + Y_\mathrm{R})\,, \tag{8}$$

where q is the heat release due to combustion.

Next, by introducing the constitutive relations (5) and (6), respectively, in the momentum and energy balance laws and by using the fact that the porosity is not a function of time, the governing system of (2)–(4) and (7) can be recast in the following form,

$$\frac{\partial\rho}{\partial t} + \nabla\cdot(\rho\boldsymbol{u}) \;=\; -\frac{\rho}{\phi}\boldsymbol{u}\cdot\nabla\phi\,, \tag{9}$$

$$\frac{\partial\rho\boldsymbol{u}}{\partial t} + \nabla\cdot(\rho\boldsymbol{u}\boldsymbol{u}) + \nabla p \;=\; -\frac{\rho}{\phi}(\boldsymbol{u}\boldsymbol{u})\cdot\nabla\phi - \frac{1}{\phi}\boldsymbol{\beta}\cdot\boldsymbol{u}\,, \tag{10}$$

$$\frac{\partial \rho e_{\mathrm{t}}}{\partial t} + \nabla \cdot ((\rho e_{\mathrm{t}} + p)\boldsymbol{u}) \;=\; -\frac{\rho e_{\mathrm{t}}}{\phi}\boldsymbol{u} \cdot \nabla\phi - \frac{1}{\phi}\left(\boldsymbol{\beta} \cdot \boldsymbol{u}\right) \cdot \boldsymbol{u} + \frac{\mathcal{E}}{\phi}\,, \tag{11}$$

$$\frac{\partial \rho Y_j}{\partial t} + \nabla \cdot (\rho \boldsymbol{u} Y_j) \;=\; \frac{\rho Y_j}{\phi}\boldsymbol{u} \cdot \nabla\phi + \frac{\dot{\omega}_j}{\phi}\,, \qquad i = \mathrm{F},\, \mathrm{R}\,. \tag{12}$$

It is worth noting that the left-hand side of the system (9)-(12) is identical to that of the compressible Euler equations. Further, since the porosity distribution ϕ is assumed to be known, the terms on the right-hand side of the system that involve the porosity gradient $\nabla\phi$ are source terms and not nonconservative products. Accordingly, the above system is strictly hyperbolic and has the same eigenvalues and eigenvectors as the compressible Euler equations. Therefore, this system admits unique weak solutions that can be computed numerically with shock-capturing algorithms for systems of hyperbolic conservation laws with with source terms. This offers a significant computational advantage because the numerical integration of hyperbolic laws with nonconservative products is quite challenging [35–37].

As regards the solid matrix, since it is assumed to be rigid and chemically inert, then its mass and momentum balance laws are identically satisfied. Further, its energy equation, derived in [33], reads in dimensionless form,

$$(1-\phi) c_{\mathrm{s}} \rho_{\mathrm{s}} \frac{\partial T_{\mathrm{s}}}{\partial t} \;=\; -(\gamma - 1)\mathcal{E}\,, \tag{13}$$

where ρ_{s} and c_{s} stand for the density and specific heat capacity of the matrix, respectively. Also, γ stands for the heat-capacity ratio of the gas.

In writing equations (9)-(13), all thermodynamic variables and transport coefficients have been nondimensionalized by the corresponding reference values of the quiescent state of the reactants F ahead of the detonation. In particular, the term $(\gamma - 1)$ appears on the right-hand side of equation (13) because c_{s} is nondimensionalized by the heat capacity under constant pressure of the reactants, while the interphasial heat exchange $\mathcal{E}$ is nondimensionalized by the pressure-to-density ratio of the reactants at the reference quiescent state.

In the above mathematical model, the microstructure of the solid matrix is taken into account via the introduction of the porosity distribution ϕ and appropriate constitutive relations for $\boldsymbol{\beta}$ and $\mathcal{E}$. Since the solid matrix is treated as a continuum, this model cannot capture the flow details at the microscopic (fibre) level. Nonetheless, for the cases where the continuum hypothesis for the solid matrix is valid, this model is deemed capable

of accurately accounting for the effects of momentum and energy exchange between the two phases, as well as for the effect of the porosity gradients. More specifically, the continuum hypothesis is valid when the diameter of the micro-elements that constitute the solid matrix is much smaller than all the relevant length scales of the flow; this is indeed the case for all the flows investigated herein.

2.1. Chemical kinetics mechanisms

In the present study we employ the following chain-branching schemes involving the 3 participating species F, R and P, plus an inert third body M,

$$\text{initiation}: \qquad \mathrm{F} \xrightarrow{\mathrm{k_i}} \mathrm{R}\,, \qquad \mathrm{k_i} = \mathrm{A_i e}^{-\frac{\mathrm{E_i}}{\mathrm{T}}}\,, \tag{14}$$

$$\text{branching}: \qquad \mathrm{F} + \mathrm{R} \xrightarrow{\mathrm{k_b}} 2\mathrm{R}\,, \qquad \mathrm{k_b} = \mathrm{A_b e}^{-\frac{\mathrm{E_b}}{\mathrm{T}}}\,, \tag{15}$$

$$\text{termination I}: \qquad \mathrm{R} \xrightarrow{\mathrm{k_{t_I}}} \mathrm{P}\,, \qquad \mathrm{k_{t_I}} = \mathrm{A_{t_I} e}^{-\frac{\mathrm{E_{t_I}}}{\mathrm{T}}}\,, \tag{16}$$

$$\text{termination II}: \qquad \mathrm{R} + 2\mathrm{M} \xrightarrow{\mathrm{k_{t_{II}}}} \mathrm{P} + 2\mathrm{M}\,, \qquad \mathrm{k_{t_{II}}} = \mathrm{A_{t_{II}} e}^{-\frac{\mathrm{E_{t_{II}}}}{\mathrm{T}}}\,. \tag{17}$$

The mechanism with the termination reaction I has been used extensively in both analytical and numerical studies of hydrogen detonations; see, for example, [3, 38–42] and references therein. The termination reaction I is favoured in high-pressure conditions because, in this case, destruction of radicals at walls is the key termination step [43, 44]. The mechanism with this termination will be referred to herein as the tI mechanism. On the other hand, at lower pressures, termination occurs mostly via collisions between radicals and the third body M [43, 44]. For this reason, the termination reaction of the type II is mostly favoured at low to moderate pressures. The mechanism involving the termination reaction II will be referred to herein as the tII mechanism.

For both mechanisms, tI and tII, the source term $\dot{\omega}_\mathrm{F}$ in the reactant mass-fraction equation (7) is given by,

$$\dot{\omega}_\mathrm{F} \;=\; -\rho\phi\left(Y_\mathrm{F} k_\mathrm{i} + \rho Y_\mathrm{F} Y_\mathrm{R} k_\mathrm{b}\right)\,. \tag{18}$$

Moreover, for the mechanism tI, the source term $\dot{\omega}_\mathrm{R}$ in the radical mass-fraction equation (7) reads,

$$\text{tI:} \qquad \dot{\omega}_{\mathrm{R_{tI}}} \;=\; \rho\phi\left(Y_\mathrm{F} k_\mathrm{i} + \rho Y_\mathrm{F} Y_\mathrm{R} k_\mathrm{b} - Y_\mathrm{R} k_{\mathrm{t_I}}\right)\,, \tag{19a}$$

whereas for the mechanism tII it reads,

$$\text{tII:} \qquad \dot{\omega}_{\mathrm{R}_{\mathrm{tII}}} \;=\; \rho\phi\left(Y_{\mathrm{F}}k_{\mathrm{i}} + \rho Y_{\mathrm{F}}Y_{\mathrm{R}}k_{\mathrm{b}} - \rho^2 Y_{\mathrm{R}}k_{\mathrm{t}_{\mathrm{II}}}\right) . \tag{19b}$$

Upon inspection of the terms in parentheses on the right-hand-sides of equations (19a) and (19b), we readily infer that the rate of termination reaction tI scales linearly with ρ, whereas that of termination reaction tII scales quadratically with ρ.

3. Numerical results

In the present study we performed simulations of gaseous detonations in 1D and 2D domains partially filled with porous media. The governing equations for the gaseous phase (9)–(12) are solved via the unsplit scheme for systems of hyperbolic conservation laws with source terms of [45, 46], whereas the energy equation of the solid matrix (13) is solved via a second-order Runge-Kutta method.

3.1. Numerical set up

In our simulations, the initial conditions consisted of ZND detonation profiles that obey one of the above chemical kinetics mechanisms. The overdrive factor, f, of a ZND detonation is defined as,

$$f \;=\; \frac{D^2}{D_{\mathrm{CJ}}^2}\,, \tag{20}$$

with D being the detonation velocity and D_{CJ} being the velocity of the corresponding CJ detonation.

In this study we considered three different cases. In the first one, labelled tIf1.1, the chemical kinetics is represented by the scheme tI, *i.e.* it employs the termination reaction I, while the overdrive factor is set to $f = 1.1$. In the second one, tIIf1.1, the overdrive is also set to $f = 1.1$ but the chemical kinetics is represented by the scheme tII, *i.e.* it employs termination reaction II. Finally, the third case, tIIf1.6, corresponds to a detonation with the kinetics scheme tII but with a higher overdrive, $f = 1.6$. The pre-exponential factors (A_{i}, A_{b} and A_{t}) and activation energies (E_{i}, E_{b} and E_{t}) of the chemical reactions for each case are provided in Table 1 below. The corresponding ZND detonation speeds D, cross-over temperatures T_{c} and von Neumann (post-shock) temperatures T_{N} are also provided in Table 1 below.

Table 1: Parameters of the numerical simulations.

Type	f	A_i	A_b	A_t	E_i	E_b	E_t	T_c	T_N	D
tIf1.1	1.1	20000	100000	3.0	20.0	15.0	0	1.44	1.4	2.28
tIIf1.1	1.1	37000	185000	1.40	20.0	15.0	0	1.27	1.4	2.28
tIIf1.6	1.6	3959	19795	0.15	20.0	15.0	0	1.27	1.6	2.75

With regard to the physical parameters of the gas, the heat-capacity ratio is set at $\gamma = 1.2$ and the heat of combustion at $q = 3.0$. The heat release q is assigned a small value and corresponds to well diluted $H_2/O_2/Ar$ mixtures. The rationale for this choice is that the effects of porous obstacles are expected to be more pronounced in diluted mixtures. Further, in diluted mixtures, the detonation velocities are moderate, which allows for shorter computational domains and, therefore, computational savings. Similarly, the dimensionless values of the activation energies are smaller than usual for purposes of computational savings and can be justified by assuming pre-heated reactants.

The cross-over temperature T_c is the temperature at which the branching and termination rates become equal. When the temperature drops below this value, the branching reaction becomes slower than the termination reaction and ignition is suppressed over long time periods [39, 40]. It is noted that for the detonation tIf1.1, the von Neumann temperature T_N is marginally smaller than T_c and, therefore, this detonation is prone to extinction [39]. In the context of our study, we conducted 1-D simulations of the evolution of this ZND wave. According to them, this detonation is subject to multi-mode instabilities but does not quench and, instead, propagates in a pulsating mode. The reason for this is that the temperature in the zone with high radical concentrations is above T_c and, therefore, the branching reaction remains faster than the termination one. The rationale for choosing case tIf1.1 is that the effect of porous obstacles is expected to be more pronounced in detonations close to extinction. On the other hand, the other two cases, tIIf1.1 and tIIf1.6 are also subject to longitudinal instabilities and propagate in a pulsating mode but the post-shock temperature always stays above T_c.

For purposes of nondimensionalization, lengths are scaled by the half-reaction length of the corresponding ZND wave, $l_{1/2}$, which is taken to be the distance between the leading shock and the point where $Y_\mathrm{P} = 0.5$. Also,

pressure and density are scaled by their values in the quiescent gas ahead of the shock, p_0 and ρ_0, respectively. Consequently, velocities are scaled by $u_\mathrm{r} = \sqrt{p_0/\rho_0}$ and time is scaled by the half-reaction time, $t_{1/2} = l_{1/2}/u_\mathrm{r}$.

With regard to the porous obstacles, the fibres that constitute the solid matrix are assumed to be identical and randomly distributed circular cylinders. Further, the cylinders are considered to be very thin (*i.e.* their diameter is very small) and normal to the plane of the flow. Accordingly, the matrix of interphasial drag parameters $\boldsymbol{\beta}$ is diagonal and, moreover, $\beta_{11} = \beta_{22}$. The coefficient β_{11} is approximated as follows. We consider the expression for the drag per unit length induced by the 2D flow around a single cylinder and multiply it by the height H and number density N_c of the cylinders,

$$N_\mathrm{c} = 4(1-\phi)/(\pi d_\mathrm{c}^2\, H)\,, \tag{21}$$

where d_c is the diameter of a single cylinder. The resulting expression reads, in dimensionless form,

$$\beta_{11} \;=\; \frac{2}{\pi}\, c_\mathrm{D}\, \frac{(1-\phi)\rho}{d_\mathrm{c}}\, |\boldsymbol{u}|\,, \tag{22}$$

and is independent of H. In the literature, various correlations for the drag coefficient c_D of arrays of circular cylinders are available; see, for instance, [47] and references therein. Generally, they are given in terms of the porosity of the medium and are applicable for a given range of cylinder Reynolds numbers, Re_c. For the types of flows considered herein, the predicted values of c_D lie between 1.2 and 1.6. In the present study, given the uncertainty of the experiments upon which these correlations are derived and for purposes of simplicity, we set $c_\mathrm{D} = 1$; this is the value of the drag coefficient for a single cylinder in the expected regime of cylinder Reynolds number Re_c.

The approximation of the interphasial heat transfer parameter is performed on the basis of the same reasoning. More specifically, we consider the expression for the rate of steady-state heat transfer across the surface of a single cylinder and we multiply it with the number density of cylinders N_s. This yields the following relation, in dimensionless form,

$$h = \frac{4(1-\phi)}{d_\mathrm{c}^2}\, \frac{\gamma}{\gamma-1}\, \frac{Nu_\mathrm{c}}{Re\, Pr}\, \kappa\,, \tag{23}$$

with κ being the dimensionless thermal conductivity of the gas. In this relation, the Reynolds and Prandtl numbers are based on the macroscopic

reference values, whereas Nu_c is the Nusselt number at the microscopic scale, *i.e.* the one that corresponds to a single cylinder. Herein we employ a well-known empirical correlation for Nu_c that is applicable for $Pr \geq 0.73$,

$$Nu_c \;=\; C\, Re_c^m\, Pr^{\frac{1}{3}}\,. \tag{24}$$

The parameters C and m of the correlation (24) depend on Re_c and their values are listed in [48].

With regard to the physical parameters of the porous medium, we assume that the cylindrical fibers of the solid matrix are made of steel with $\rho_s = 6800\,\rho_0$ and specific heat $c_s = 2.2\,R$, with R being the gas constant of the reactive mixture. Also, the diameter of the cylinders is set to $d_c = 0.05\,l_{1/2}$.

In all the simulations of the present study, the initial condition is the profile of the corresponding ZND wave. This profile is placed in front of the first porous block which is located 5 $l_{1/2}$ downstream from the inflow boundary. The thermodynamic variables and velocity of the gas at the end of the reaction zone, marked by $Y_R = 1.0$, are assigned at the rear inflow boundary. In this manner, the overdrive of a given ZND profile that is used as initial condition, is supported by the corresponding inflow condition at the rear boundary.

In the simulations, the resolution of the computational grid is 50 points per $l_{1/2}$. According to grid-convergence analysis conducted in the context of our study, this resolution is deemed sufficient to capture the relevant flow structures and produce well-resolved results. Finally, the simulations have been performed with a Courant number equal to 0.7.

3.2. Single porous section

First, we present results from one-dimensional simulations of detonation attenuation by a single porous section, *i.e.* an obstacle that spans the entire cross section of the channel. The length of the porous section is set equal to 10 $l_{1/2}$. Simulations have been performed with all three different detonation types mentioned above and with porosity ranging from $\phi = 0.80$ to $\phi = 0.98$.

Our simulations predicted that as soon as the detonation wave enters the porous section, a reflected shock is formed that moves upstream, thereby raising the pressure and temperature of the reacted gas close to the rear boundary. As the detonation wave propagates through the porous medium, the strength of the leading shock is reduced due to interphasial drag, as expected. This, in turn, results in lower temperatures and, therefore, lower

radical concentrations, burning rates and detonation velocities. Nonetheless, once the leading shock exits the porous section, its strength is stabilised.

At the same time, the combustion zone is advected at lower velocities and its distance from the leading shock decreases. However, the temperature inside this zone stays higher than the cross-over temperature T_c and, as a result, the branching reaction remains faster than the termination one. This holds true even for the detonation tIf1.1; in this particular case the temperature at the point of maximum radical concentration is 1.5, which is just above T_c. Consequently, the radical concentration inside the reaction zone increases with time. This is accompanied by the increase of both temperature and pressure in the vicinity of the reaction zone, which also leads to a slow increase of the leading-shock pressure ahead. Eventually, the radical concentration passes a certain threshold, which signals the re-establishment of the rapid burning of reactants and the onset of a chain-branching explosion. This explosion produces two pressure waves, one travelling upstream and one downstream, respectively. The downstream-travelling wave evolves to a shock which ignites the material that it bypasses and eventually reaches the precursor shock, thereby re-initiating the detonation.

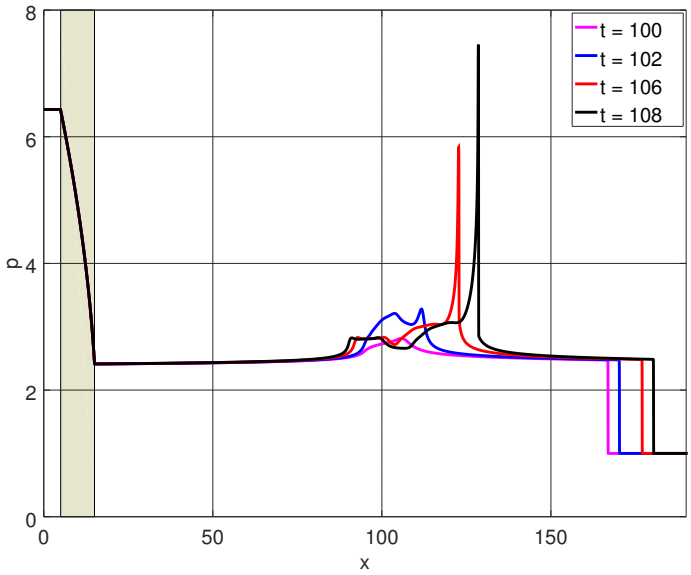

Figure 1: Pressure profiles at different time instances that depict the re-ignition process of the detonation tIIf1.1 downstream of a single porous section of $\phi = 0.95$. The shaded area marks the extent of the porous section, the length of which is 10 $l_{1/2}$.

In Figure 1, we present plots of the pressure field at different time instances for the detonation tIIf1.1. The porosity of the porous section in this simulation is $\phi = 0.95$. In this figure we can clearly observe the monotonic decrease of the pressure inside the porous medium and the formation of the pressure wave from the chain-branching explosion which re-ignites the detonation.

Also, for the same case (detonation tIIf1.1 and $\phi = 0.95$), in Figure 2 we present plots of the flow variables in the vicinity of the chain-branching explosion. More specifically, this figure shows plots of the pressure p, temperature T, reactant concentration Y_{F} and radical concentration Y_{R} at different time instances. Therein, one can observe the gradual build-up of radicals which is accompanied by the simultaneous increase of pressure and temperature. This leads to the aforementioned chain-branching explosion and the formation of the shock wave that eventually re-initiates the detonation.

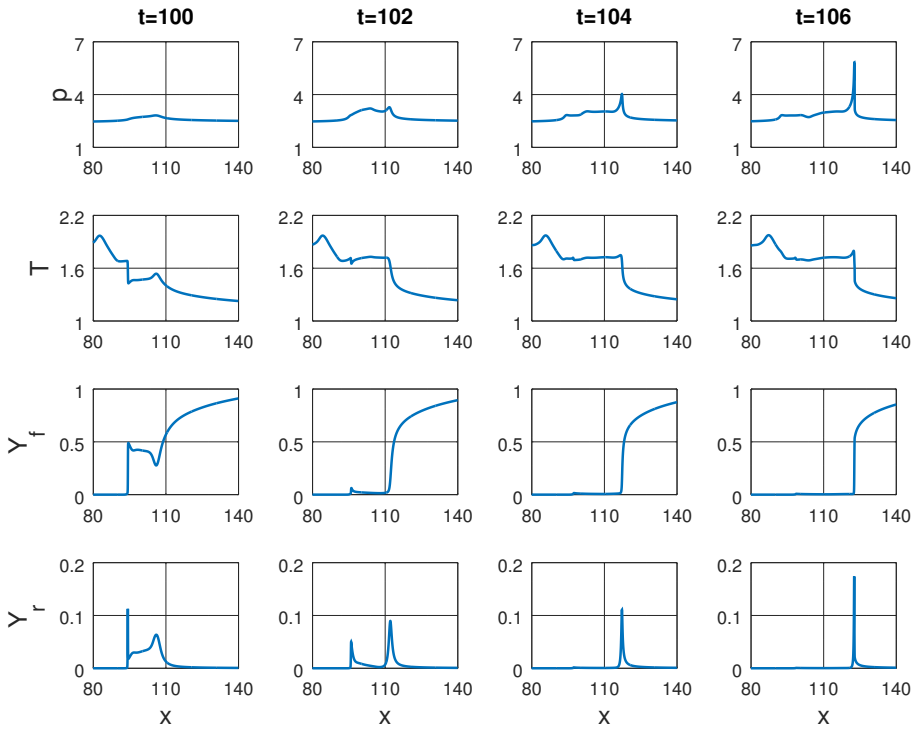

Figure 2: Profiles of flow variables at different time instances that depict the chain-branching explosion that causes the re-ignition of the detonation tIIf1.1 downstream of a single porous section. The porosity of the section is $\phi = 0.95$ and its length is 10 $l_{1/2}$.

These observations have been corroborated by simulations with the other two types of detonations considered herein, tIf1.1 and tIIf1.6. According to them, the detonations always re-ignite at a certain distance from the porous section. Additionally, we have performed simulations with longer porous media, namely, 15 and 20 $l_{1/2}$ long. In all cases, the detonations re-initiate downstream of the porous section, independently of the type of detonation or length of the porous section. Also, our simulations predicted that the re-initiation time, t_{r}, and distance, l_{r}, increase monotonically with the length of the porous section, as expected.

Within the framework of our investigations, we have also performed a parametric study of the re-initiation time and distance with respect to the porosity ϕ. The results of this study for the detonations tIf1.1, tIIf1.1 and tIIf1.6, respectively, are presented in Figures 3, 4 and 5. For the porosity range considered herein, $0.80 \leq \phi \leq 0.98$, both t_{r} and l_{r} decrease linearly with the porosity ϕ for detonations tIf1.1 and tIIf1.1, *i.e.* when the overdrive factor is $f = 1.1$.

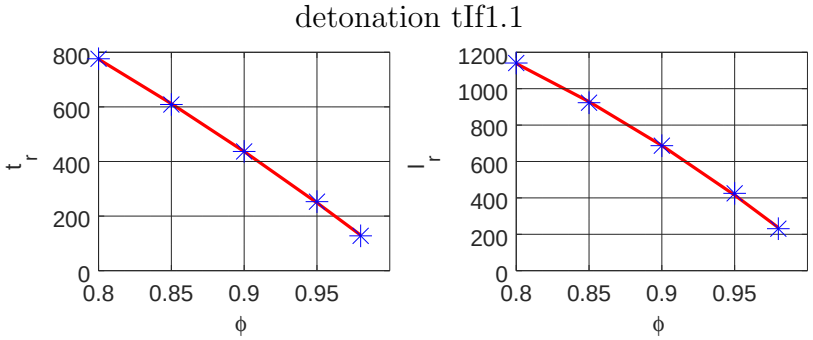

Figure 3: Attenuation of the detonation tIf1.1 by a single porous section: variation of the re-initiation time t_{r} and distance l_{r} with porosity. The length of the porous section is 10 $l_{1/2}$. Left: t_{r}. Right: l_{r}. The star symbol corresponds to the numerical results and the line to a least-squares fit.

Further, upon comparison of the plots in Figures 3 and 4, we may infer that the termination reaction I results in proportionally longer re-initiation times and distances. Moreover, the slopes of the curves $t_{\mathrm{r}}(\phi)$ and $l_{\mathrm{r}}(\phi)$ are steeper for the detonation tIf1.1. In other words, the rate at which t_{r} and l_{r} decrease with the porosity is higher when the termination reaction is of type I. This is attributed to the higher dependence of the radical concentration Y_{R} on the gas density in the termination reaction II. Indeed, according to the

right-hand sides of equations (19a) and (19b), respectively, Y_{R} scales with ρ^2 for termination I and with ρ^3 for termination II.

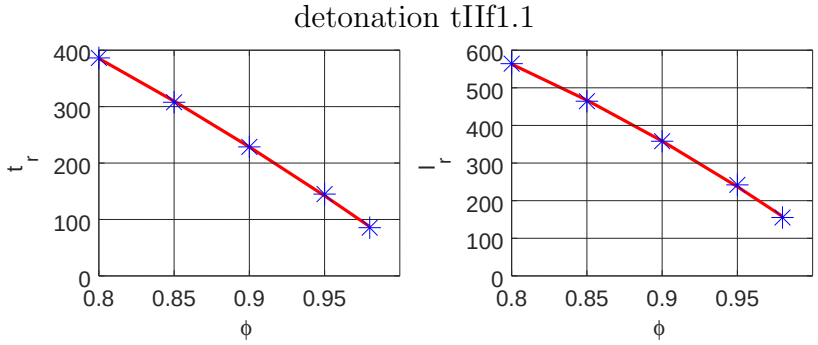

Figure 4: Attenuation of the detonation tIIf1.1 by a single porous section: variation of the re-initiation time t_{r} and distance l_{r} with porosity. The length of the porous section is 10 $l_{1/2}$. Left: t_{r}. Right: l_{r}. The star symbol corresponds to the numerical results and the line to a least-squares fit.

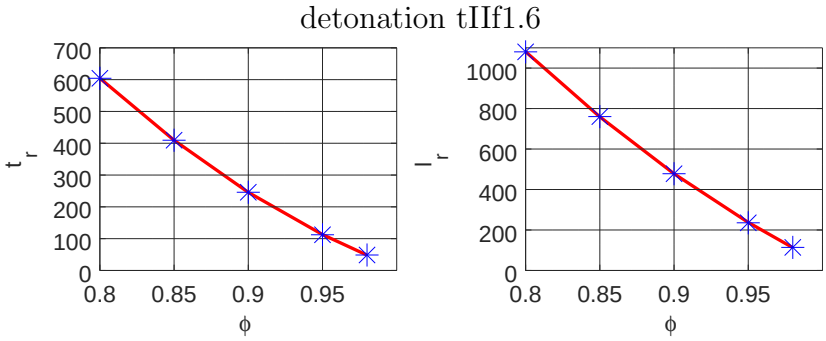

Figure 5: Attenuation of the detonation tIIf1.6 by a single porous section: variation of the re-initiation time t_{r} and distance l_{r} with porosity. The length of the porous section is 10 $l_{1/2}$. Left: t_{r}. Right: l_{r}. The star symbol corresponds to the numerical results and the line to a least-squares fit.

On the other hand, for the detonation with high overdrive, tIIf1.6, the variation of t_{r} and l_{r} with ϕ is better approximated by a quadratic curve than with a linear one. Moreover, the slopes of $t_{\mathrm{r}}(\phi)$ and $l_{\mathrm{r}}(\phi)$ are steeper for this detonation. In other words, as the overdrive factor and the strength of the detonation increase, so does the sensitivity of t_{r} and l_{r} with the porosity ϕ. Also, upon comparison of the plots in Figures 4 and 5, we may infer that the stronger detonation, *i.e.* the one with the higher overdrive, has shorter

re-initiation time t_r, as expected. (Note that the half-reaction time $t_{1/2}$ of tIIf1.6 is much shorter than that of tIIf1.1, as is evidenced by the fact that the pre-exponential factors for tIIf1.6 are much smaller than those of tIIf.1.)

The above discussion on detonation re-initiation refers to cases in which the re-initiation time is sufficiently short so that heat losses due to interphasial heat transfer do not play a significant role. However, when the re-initiation times become too long (for example, by employing much longer porous sections), then these heat losses may actually prevent the re-initiation of the detonation.

3.3. Array of porous sections

In this subsection we present 2D simulations of detonation attenuation by a perpetual array of porous sections. The length of each porous section is kept at 10 $l_{1/2}$ and the distance between neighboring sections is 20 $l_{1/2}$. In other words, the flow domain consists of alternating pure-fluid and porous sections, each one of them being 10 $l_{1/2}$ long. The width of the computational domain is 10 $l_{1/2}$ and periodic conditions are imposed at the lateral boundaries.

In an unobstructed channel of such width, the ZND detonations mentioned above develop cellular patterns whose cell size is equal to the channel width. In other words, there is one cell per period. On the other hand, our simulations predicted that, in the presence of a perpetual array of porous sections, the flow structure remains essentially one-dimensional. In other words, the variations of the flow quantities and detonation properties in the transversal direction are negligible. This is due to the fact that the porous sections suppress transversal instabilities.

Further, the array of porous sections causes the suppression of the detonation no matter how high their porosity ϕ is. More specifically, the strength of the leading shock attenuates significantly with time and the distance between the reaction zone and the leading shock increases with time. In other words, the porous obstacles cause the decoupling of the detonation into a shock of decreasing strength and a (slower-moving) subsonic flame.

Figure 6 shows the history of the shock pressure, p_s, for the detonation tIIf1.1 and porous sections of porosity $\phi = 0.95$. According to it, the decrease of the shock pressure is not monotonic but is modulated by the alternation of porous and pure-fluid zones. In particular, when the shock passes through a porous section, p_s decreases. Equivalently, when it passes through a pure-fluid section, p_s increases albeit moderately.

Also, in Figure 7 we provide plots of the profiles of the gas pressure p and reactant concentration $Y_{\rm F}$ at three different times for the same case, *i.e.* detonation tIf1.1 with porous sections of porosity $\phi = 0.95$. These plots confirm that the distance between the reaction zone and the precursor shock increases with time, despite the high porosity of the porous sections. Further, these plots reaffirm that the shock pressure decreases strongly inside the porous sections and mildly in the pure-fluid ones, as mentioned above. Interestingly, in the same figure and in the plot for $t = 20$, we discern a shock wave located at $x \approx 22$ that propagates upstream. This is the reflected shock that was formed when the leading shock entered the second porous obstacle.

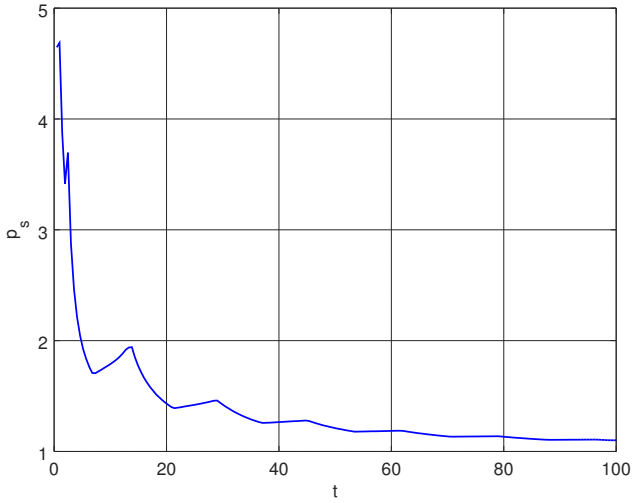

Figure 6: Attenuation and suppression of the detonation tIIf1.1 by an array of porous sections with porosity $\phi = 0.95$. The plot shows the evolution of the shock pressure $p_{\rm s}$ with time. The segments of the plot in which $p_{\rm s}$ decreases correspond to the time intervals that the precursor shock is located inside a porous section. Equivalently, the segments in which $p_{\rm s}$ increases correspond to the time intervals that the precursor shock is located in a pure-fluid unobstructed region.

The detonation suppression is caused by the interphasial force $\beta_{11}u$ which plays the role of a momentum sink for the gas. Due to this force, when the leading shock passes through a porous section, its strength decreases. This results in lower temperatures behind the shock. Consequently, the material behind the leading shock does not burn rapidly and therefore the combustion zone detaches from the shock and stays at its wake. The reaction zone is then

advected by the flow and its distance from the leading shock increases with time. Nonetheless, the temperature inside the reaction zone is still higher than the cross-over temperature T_c and, therefore, the radical concentration builds up, thereby leading to chain-branching explosions. In Figure 7 we can infer that such an explosion has started at $t = 40$ and in the vicinity of low reactant concentration Y_F, at $x \approx 37.5$.

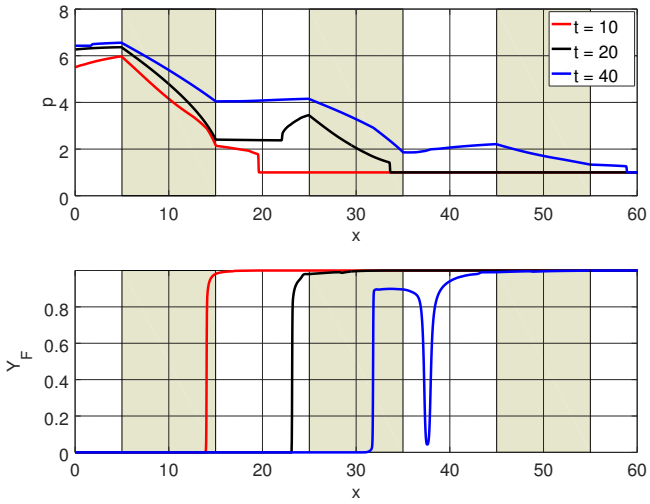

Figure 7: Attenuation and suppression of the detonation tIIf1.1 by an array of porous sections with porosity $\phi = 0.95$: pressure and reactant concentration profiles at different time instances. Top: pressure p. Bottom: reactant-concentration Y_F. The shaded areas mark the porous sections.

However, the pressure waves that are produced from these explosions attenuate rapidly once they enter a porous section. As a result, they never reach the leading shock which continues to attenuate and eventually reduces to an acoustic discontinuity. The evolution of a pressure wave created by a chain-branching explosion is depicted in Figure 8 which clearly shows its rapid attenuation once it enters the porous section ahead of it.

The combustion behind the leading shock does not extinguish because the temperature is sufficiently high to maintain the production of radicals. Consequently, the combustion zone is advected by the flow and propagates at subsonic speeds, which implies that its distance from the leading shock increases with time. In other words, the porous sections keep the combustion zone separated from the leading shock. Thus, the detonation is suppressed

not because the combustion is shut off but because the distance of the reaction zone from the shock increases with time. This is an example of detonation suppression via mechanical (as opposed to chemical or thermal) means. Such a detonation decoupling into a leading shock and a fast subsonic flame has also been reported in recent experiments on a rather different setting, namely, detonation attenuation via highly porous wall coatings [26].

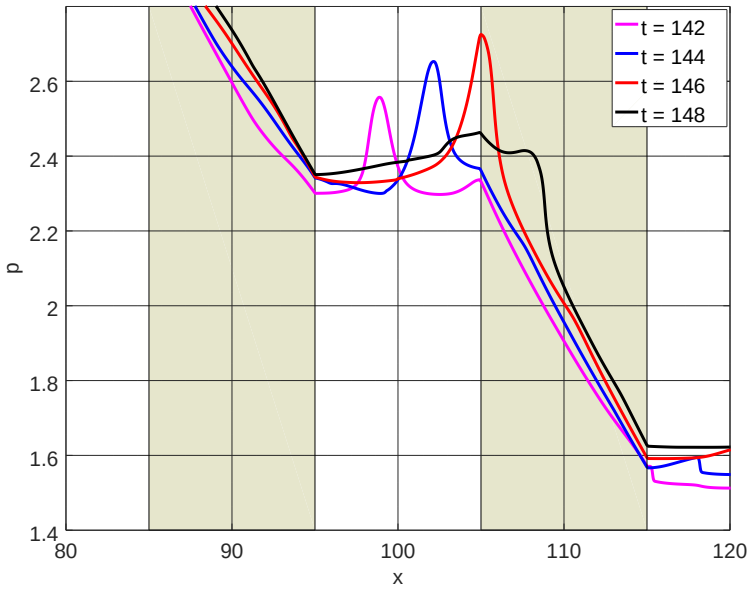

Figure 8: Attenuation and suppression of the detonation tIIf1.1 by an array of porous sections with $\phi = 0.95$: evolution of the pressure waves created by a chain-branching explosion. At $t = 146$ the explosion is located at $x \approx 100.5$. The pressure waves attenuate rapidly once the enter a porous section (black line). The shaded areas mark the porous sections.

During our study, we performed additional simulations with increased spacing between the porous sections, namely 15 and 20 $l_{1/2}$. These simulations predicted that the detonations still get suppressed despite the increased spacing. The reason for this is that the detonation attenuation inside the porous sections is far too strong for the shock to regain its strength in the intervening pure-fluid zones. In fact, on the basis of our simulations, we may conjecture that for the detonation to re-ignite, the spacing between the porous sections should be at the order of the re-initiation length l_{r} (mentioned above) for a detonation passing through a single porous section.

Finally, it is worth adding that, according to our simulations, the inter-

phasial heat exchange plays no role in the evolution of the detonations. This is mainly due to the small value of the gas conductivity and the large value of the macroscopic Reynolds number Re that enter equation (23). Thus, the characteristic time-scale of the interphasial heat exchange is too long with respect to the hydrodynamic time-scale and consequently it has not effect on the dynamics of the flow. In other words, the attenuation of detonations by porous media is due to purely mechanical effects and heat losses do not contribute to it. This is in contrast to the role of the interphasial heat exchange in particle-laden detonations, which can be considerable [49, 50].

3.4. Biperiodic array of porous blocks

In this subsection we present and analyze 2D simulations of detonation attenuation by a biperiodic array of porous blocks. The dimensions of each block are $10 \times 5\, l_{1/2}$, which means that the porous obstacles do not span the entire width of the channel. The streamwise distance between the centers of neighboring block is set at 20 $l_{1/2}$. As in the simulations of the previous subsection, the width of the computational domain is 10 $l_{1/2}$ and periodic conditions are applied along the lateral boundaries. Herein, we present results for the detonation tIIf1.1. Two cases with different values of the porosity of the blocks have been considered, namely, $\phi = 0.95$ and $\phi = 0.98$.

According to our simulations, the fact that the porous blocks do not span the entire width of the channel signifies that the detonation wave does not quench. In other words, the unobstructed pathways that are available to the fluid particles render the detonation sustainable, at least for the duration of the simulations. Nonetheless, the force exerted by the solid matrix on the gas still has a profound effect on the evolution of the detonation wave.

The shock-pressure histories at the lower periodic boundary $y = 0$ for these two cases are shown in Figure 9. According to these plots, once the detonation enters the first block, the shock pressure drops significantly, to approximately half the value of the corresponding ZND wave. Subsequently, the detonation propagates down the channel in an oscillatory mode. The frequency and amplitude of the shock-pressure oscillation are modulated by the porous blocks. For the two cases examined herein, the amplitude of the oscillation is approximately 40% of the mean (time-averaged) value of the shock pressure.

It is noted that the leading-shock pressure is considerably lower than the maxima of the pressure field; the latter ones correspond to reflected shocks that are formed upon incidence of the leading shock on the porous

obstacles. Further, in Figure 9 one can observe that the mean shock pressure is mildly lower for $\phi = 0.98$ than for $\phi = 0.95$, as one would expect. However, the oscillation frequency of the shock pressure is almost the same in the two cases, which corroborates the fact that it is mainly controlled by the distance between neighboring porous blocks. Further, the oscillation of the shock pressure is characterized by very steep increases followed by long time periods of attenuation. These long periods of attenuation correspond to the passing of the leading shock through obstructed sections, whereas the sharp peaks occur in the unobstructed sections. In fact, the oscillation of the leading shock is reminiscent to those of quasi-detonations in tubes with a dense array of obstacles in [14]. However, as is explained below, there is an important difference between the low-velocity detonations predicted herein and quasi-detonations in tubes with solid obstacles.

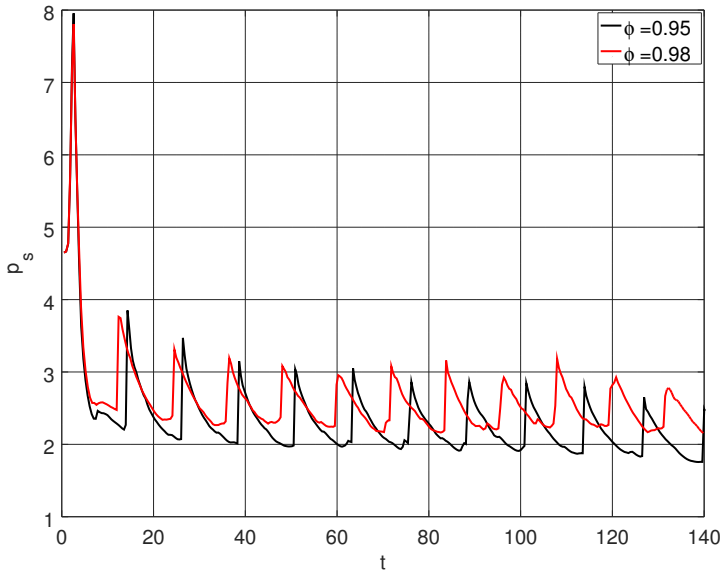

Figure 9: Attenuation of the detonation tIIf1.1 by a biperiodic array of porous blocks: shock pressure histories at $y = 0$ for blocks with $\phi = 0.95$ and $\phi = 0.98$, respectively.

Contour plots of the pressure p and reactant concentration Y_{F} for three different time instances are plotted in Figure 10. The most striking feature is that the main reaction front is kept at a distance from the leading shock. This is due to the attenuation of the shock which results in lower post-shock temperatures and, therefore, ignition delays. Another important feature is

that the reaction zone decelerates inside the porous blocks due to the interphasial force and, consequently, is stretched along their lateral boundaries.

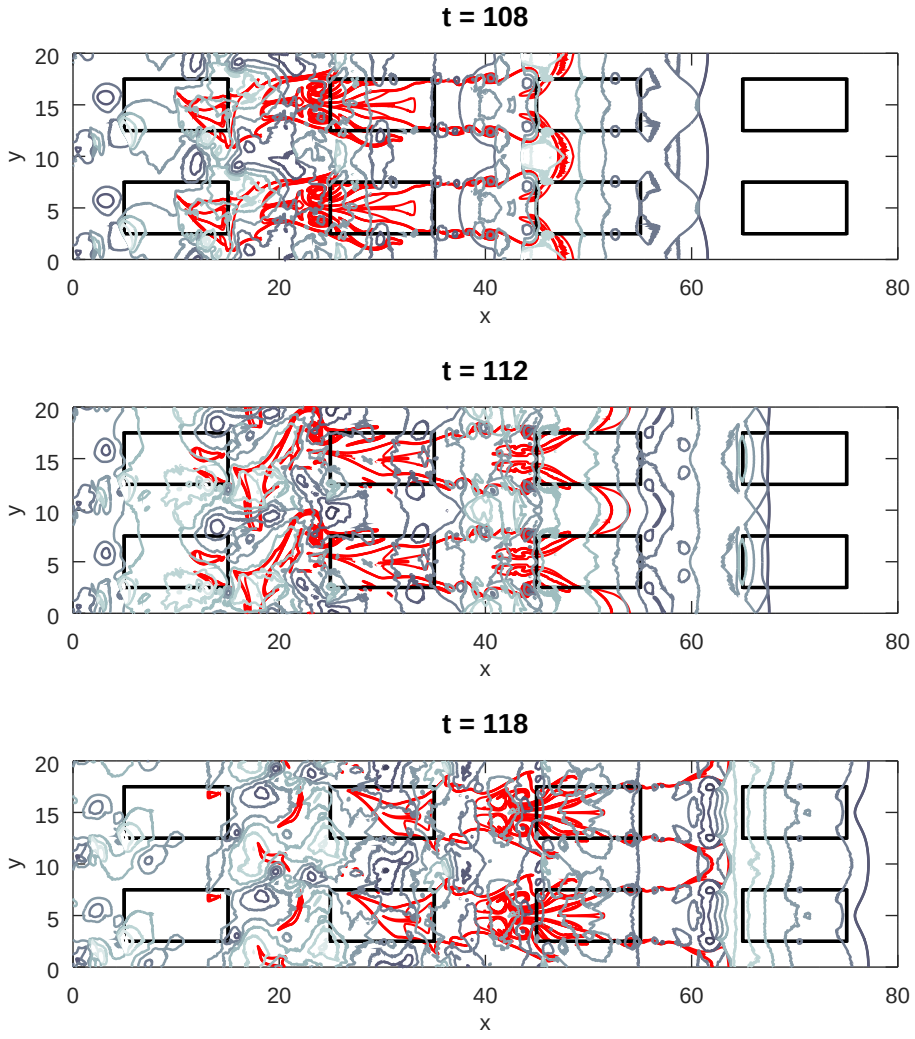

Figure 10: Attenuation of the detonation tIIf1.1 by a biperiodic array of porous blocks with $\phi = 0.95$: contour plots of the pressure (blue lines) and reactant mass fraction Y_{F} (red lines) at different time instances. The embedded rectangles mark the porous blocks. Two periods in the y direction are shown. The pressure maxima at $t = 108$, 112 and 118 are $p = 4.75$, 4.54 and 4.65, respectively, and correspond to reflected shocks that propagate upstream.

Also, from Figure 10 we infer that the leading shock attains the typical

cellular structure when it propagates in an unobstructed section of the channel. This structure is characterized by high shock curvature and triple points that move along the shock and collide with each other. On the contrary, in the obstructed sections, both the leading shock and the transverse shocks emanating from its triple points attenuate. As a result, the leading shock loses almost all of its curvature and essentially flattens out. The attenuation of transversal shocks has been identified as a key factor to the quenching of detonations, including those in channels with porous wall coatings [27, 28]. In the flow under study, the suppression of the transversal instabilities and shocks is temporary because once the leading shock exits a porous block, then triple points are formed in a very short time. Nonetheless, due to the low activation energy and heat release (resulting from the preheating of the reactants) the transverse shocks are weak and, therefore, their impact on the propagation of the detonation is reduced.

Despite their efficiency as momentum sinks, the porous blocks do not absorb enough momentum from the gas to prevent the re-establishment of the detonation cellular structure, at least for the range of porosity examined herein. As a result, the detonation does not quench but, instead, the combined system of leading shock and combustion zone propagates in the form of a low-velocity detonation. For $\phi = 0.95$, the mean (time-averaged) detonation velocity is $D \approx= 1.6$, which is approximately 70% of the corresponding ZND velocity given in Table 1. Similarly, for $\phi = 0.98$ the mean detonation velocity is approximately 75% of the corresponding ZND one.

However, there is an important difference between the low-velocity detonations predicted herein and quasi-detonations in tubes with solid obstacles. More specifically, as mentioned in the introduction, quasi-detonations due to solid obstacles are sustained via re-ignitions due to reflections of the diffracted transverse shocks from the tube walls. But as mentioned above, the reflected shocks in the flows under study are not particularly strong. Moreover, due to the high porosity of the obstacles, their reflections are even weaker. As a result, the reflected transverse waves cannot raise the temperature sufficiently so as to generate chain-branching explosions in the wake of the leading shock. Further, they attenuate rapidly inside the porous blocks that they encounter. Instead, the reflected shocks contribute to the slow rise of the temperature of the unreacted gas in the unobstructed regions and to the establishment a combustion zone albeit with a certain ignition delay. As a result, the combustion front is maintained at a certain distance from the leading shock, as can be readily seen in Figure 10.

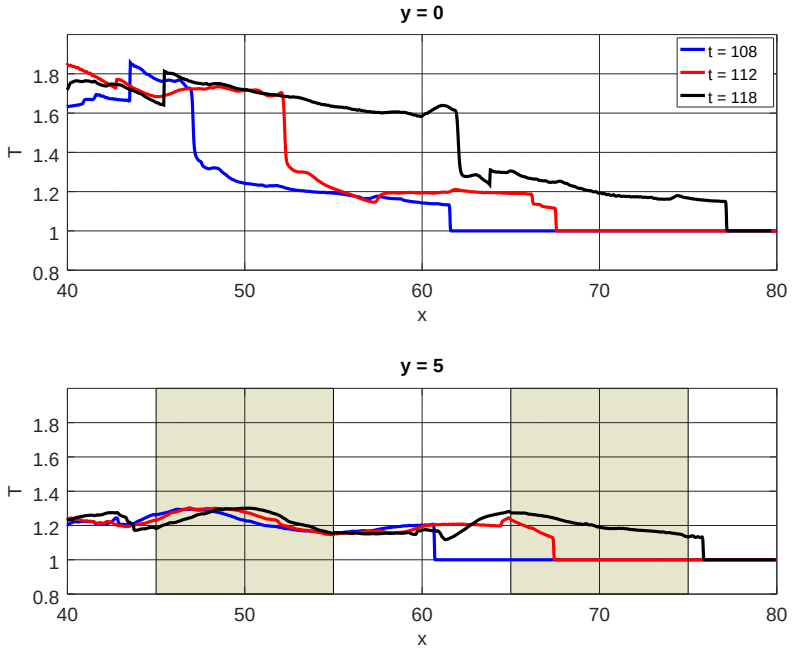

Figure 11: Attenuation of the detonation tIIf1.1 by a biperiodic array of porous blocks of $\phi = 0.95$: temperature profiles along two different horizontal axes. Top: profile along the line $y = 0$ which is unobstructed, *i.e.* it does not "cut through" a porous block. Bottom: profile along the line $y = 5$ which cuts through a porous block. The shaded areas mark the porous blocks. The time instances are the same as those considered in Figure 10.

Additional information about this process can be provided by the temperature profiles shown in Figure 11. The top part of this figure shows temperature profiles along the horizontal line $y = 0$ which is unobstructed, *i.e.* it does not "cut through" the series of porous blocks. The bottom part shows temperature profiles along the line $y = 5$ which cuts through the arrays of porous blocks. We observe that along unobstructed lines, the shock temperature is below the cross-over temperature $T_c = 1.27$ but rises slowly as the distance behind the shock increases. Combustion is initiated at the points where the temperature surpasses T_c. The main reaction zone is located at approximately 15 $l_{1/2}$ behind the leading front, and is marked by the sharp temperature gradient. On the other hand, along lines that cut through the porous blocks, the temperature stays below T_c over much longer distances behind the leading shock, approximately 30 $l_{1/2}$. The reason for this is the deceleration of the combustion front inside porous blocks due to interphasial drag. Moreover, the reflected shocks in the wake of the leading

front attenuate rapidly once they enter a porous block and, therefore, cannot increase the temperature (hence the burning rate) of the gas located therein.

Finally, in Figure 12 we present contour plots of the vorticity field and the radical concentration Y_{R} for the case with $\phi = 0.95$; they correspond to the third plot of Figure 10. According to this figure, the vorticity distribution inside the porous blocks is minimal due to the force exerted by the solid matrix on the gas which suppresses the flow instabilities. On the other hand, large vortical structures are present in the pure-fluid regions in the wake of the leading front. Initially, they are part of the vortex sheets that emanate from the triple points of the leading shock. Once they encounter a porous block, these large vortices detach from the shock, go around the block and interact with other vortical structures. Also, these vortices stretch the pockets of partially unreacted material and break them into smaller ones. This results in an increase of the overall reaction surface area.

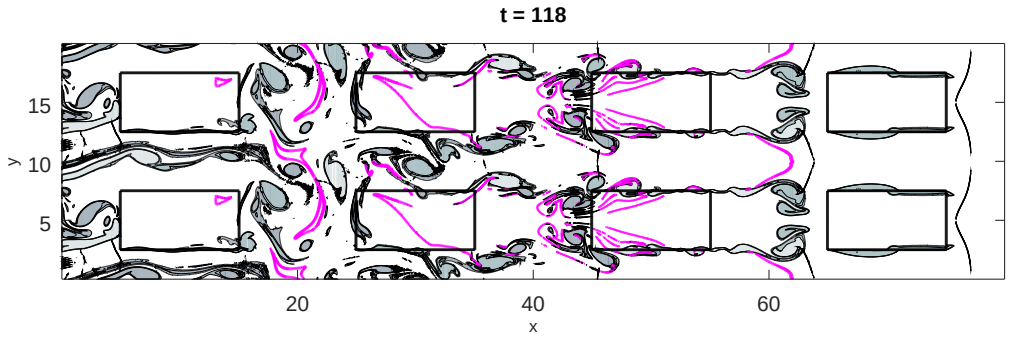

Figure 12: Attenuation of the detonation tIIf1.1 by a biperiodic array of porous blocks of $\phi = 0.95$: contour plots of the absolute value of vorticity and radical concentration Y_{R} (magenta lines). The time instance is the same as in the bottom plot of Figure 10. The embedded rectangles mark the porous sections. Two periods in the y direction are shown. The figure contains 5 equally spaced contours of Y_{R} between 0 and the maximum value $Y_{\mathrm{R}} = 0.294$ and 5 equally spaced contours of the absolute value of vorticity between the values 0.5 and 1.2.

With regard to Figure 12, it is worth observing that the difference in the streamwise velocities inside and outside a porous block, leads to the formation of shear layers along the lateral boundaries of the blocks. These shear layers become unstable very quickly and interact with the vortex sheets of the leading front, which tends to increase the reaction surface area as well. The formation of such shear layers has been reported in combustion experiments in horizontal partially-filled channels [51]. In incompressible

flows, the formation and evolution of shear layers at the interfaces between porous and pure-fluid regions is well documented [52], whereas the dynamics of equivalent compressible shear layers are less understood.

4. Concluding remarks

In this article, the attenuation of gaseous detonations in channels that contain porous obstacles of fine microstructure has been studied via direct numerical simulations. This study was based on a thermo-mechanical model for flows in superposed porous and pure-fluid regions. According to it, the solid matrix is represented as a rigid continuum, the porosity of which is introduced as a distribution parameter. With regard to chemical kinetics, we employed two different three-step chain-branching schemes. The difference between them lies on the termination reaction; the rate of the termination reaction in the first scheme scales linearly with the gas density, whereas that of the second one scales quadratically.

The basic mechanism for the attenuation of detonations is the interphasial force exerted by the solid matrix which acts as a momentum sink for the gas. By contrast, the effect of the interphasial heat exchange is negligible. The simulations predicted that a single porous section, *i.e.* a partial blockage that spans the cross section of the channel, attenuates substantially the detonation, even at very high porositites. Nonetheless, once the detonation exits the porous section, it re-initiates at some distance from it. At low overdrives, both the re-initiation distance and time decrease linearly with the porosity, whereas at high overdrives, their decrease scales quadratically with the porosity. Also, according to the simulations, the detonation re-initiation occurs faster with the second termination reaction than with the first one. This is attributed to the fact that the rate of the second termination reaction has a higher dependence on the gas density.

On the other hand, an array of porous sections always causes the suppression of the detonation. This is due to the perpetual decrease of the shock strength and the low post-shock temperatures that such a decrease entails, which results in a decoupling of the detonation in a shock of decreasing strength and a subsonic flame.

Further, our simulations predicted that biperiodic arrays of porous blocks do not quench the detonation, at least for the duration of our simulations, but nonetheless slow it down significantly. The shock pressure oscillates in a manner similar to quasi-detonations propagating in tubes with dense

solid obstacles. However, in the flows examined herein and in contrast to quasi-detonations, there are no re-initiation events caused by reflections of transverse shock waves. Instead, the main reaction front is able to follow the leading shock albeit at a certain distance from it. The combined shock-reaction zone system propagates at speeds that are much lower than that of the corresponding ZND wave.

References

[1] I. O. Moen, S. A. Ward, P. Thibaut, J. H. S. Lee, R. Knystautas, T. Dean, C. K. Westbrook, The influence of diluents and inhibitors on detonations, P. Combust. Inst. 185 (1984) 1717–1725.

[2] F. Evariste, M. Lefebvre, P. J. V. Tiggelen, Inhibition of detonation wave with halogenated compounds, Shock Waves 6 (1996) 233–239.

[3] M. V. Papalexandris, Numerical study of detonation transmission in mixtures containing chemical inhibitors, Physics of Fluids 24 (2012) 056102.

[4] B. Zhang, N. Mehrjoo, H. D. Ng, J. H. S. Lee, C. Bai, On the dynamic detonation parameters in acetylene–oxygen mixtures with varying amount of argon dilution, Combust. Flame 161 (2014) 1390–1397.

[5] M. Arienti, J. E. Shepherd, A numerical study of detonation diffraction, J. Fluid Mech. 529 (2005) 117—-146.

[6] M. V. Papalexandris, J. F. Thomas, C. Jacobs, V. Deledicque, Structural characteristics of detonation expansion from a small channel to a larger one, P. Combust. Inst. 31 (2) (2007) 2407–2414.

[7] R. Sorin, R. Zitoun, B. Khaisanov, D. Desbordes, Detonation diffraction through different geometries, Shock Waves 19 (2009) 11–23.

[8] F. Pintgen, J. Shepherd, Detonation diffraction in gases, Combust. Flame 156 (3) (2009) 665–677.

[9] C. W. Kauffman, Y. Chuanjun, J. A. Nicholls, Gaseous detonations in porous media, Symposium (International) on Combustion 19 (1) (1982) 591–597.

[10] A. Teodorczyk, J. H. S. Lee, R. Knystautas, Propagation mechanism of quasi-detonations, Symposium (International) on Combustion 22 (1) (1989) 1723–1731.

[11] I. Brailovsky, G. Sivashinsky, Effects of momentum and heat losses on the multiplicity of detonation regimes, Combust. Flame 128 (1–2) (2002) 191–196.

[12] F. Togashi, R. Lohner, N. Tsuboi, Numerical simulation of H2/air detonation wave around obstacles using detailed reaction models, 44th AIAA Aerospace Sciences Meeting and Exhibit (2006) 2006–954.

[13] I. Brailovsky, G. Sivashinsky, Hydraulic resistance and multiplicity of detonation regimes, Combust. Flame 122 (1-2) (2000) 130–138.

[14] J. P. Dionne, H. D. Ng, J. H. S. Lee, Transient development of friction-induced low-velocity detonations, P. Combust. Inst. 28 (1) (2000) 645–651.

[15] S. Medvedev, S. V. Khomik, B. E. Gelfand, Recovery and suppression of the detonation of hydrogen-air mixtures at an obstacle with orifices, Russ. J. Phys. Chem. B 3 (9) (2009) 963–970.

[16] C. K. Chan, D. R. Greig, The structures of fast deflagrations and quasi-detonations, Symposium (International) on Combustion 22 (1) (1989) 1733–1739.

[17] B. Zhang, H. Liu, The effects of large scale perturbation-generating obstacles on the propagation of detonation filled with methane–oxygen mixture, Combust. Flame 182 (2017) 279–287.

[18] M. Kellenberger, G. Ciccarelli, Advancements on the propagation mechanism of a detonation wave in an obstructed channel, Combust. Flame 191 (2018) 195–209.

[19] G. Rainsford, J. S. A. Deepinder, G. Ciccarelli, Visualization of detonation propagation in a round tube equipped with repeating orifice plates, Combust. Flame 198 (2018) 205–221.

[20] X. Sun, Q. Li, S. Lu, The propagation mechanism of detonation wave in a round tube filled with larger blockage ratio orifice plates, Int. J. Hydrogen Energ. 44 (14) (2019) 7684–7691.

[21] M. Kellenberger, G. Ciccarelli, Three-dimensional behaviour of quasi-detonations, Combust. Flame 215 (2020) 145–156.

[22] A. Makris, H. Shafique, J. H. S. Lee, R. Knystautas, Influence of mixture sensitivity and pore size on detonation velocities in porous media, Shock Waves 5 (1995) 89–95.

[23] M. I. Radulescu, J. H. S. Lee, The failure mechanism of gaseous detonations: experiments in porous wall tubes, Combust. Flame 131 (2002) 29–46.

[24] T. Slungaard, T. Engebretsen, O. Sønju, The influence of detonation cell size and regularity on the propagation of gaseous detonations in granular materials, Shock Waves 13 (2003) 13–308.

[25] G. Ciccarelli, Explosion propagation in inert porous media, Phil. Trans. R. Soc. A 370 (2012) 647–667.

[26] G. Bivol, S. V. Golovastov, V. V. Golub, Detonation suppression in hydrogen–air mixtures using porous coatings on the walls, Shock Waves 28 (2018) 1011–1018.

[27] G. Bivol, S. V. Golovastov, V. V. Golub, Effects of the pore size on hydrogen–air detonation propagation in the channel with porous walls, J. Phys.: Conf. Ser. 1147 (2019) 012046.

[28] G. Bivol, S. Golovastov, Effects of polyurethane foam on the detonation propagation in stoichiometric hydrogen-air mixture, Process Saf. Environ. 130 (2019) 14–21.

[29] F. Zhang, J. H. S. Lee, Friction-induced oscillatory behaviour of one-dimensional detonations, Proc. Roy. Soc. A 446 (1994) 87–105.

[30] L. S. Gu, R. Knystautas, J. H. S. Lee, Influence of obstacle spacing on the propagation of quasi-detonation, Dynamics of Explosions; Progress in Astronautics and Aeronautics 114 (1988) 232–247.

[31] V. Bykov, I. Goldfarb, V. Goldshtein, L. Kagan, G. Sivashinsky, Effects of hydraulic resistance and heat losses on detonability and flammability limits, Combust. Theor. Model. 8 (2) (2004) 413–424.

[32] M. I. Radulescu, B. Maxwell, The mechanism of detonation attenuation by a porous medium and its subsequent re-initiation, J. Fluid Mech. 667 (2011) 96—-134.

[33] M. V. Papalexandris, P. D. Antoniadis, A thermo-mechanical model for flows in superposed porous and fluid layers with interphasial heat and mass exchange, Int. J. Heat Mass Tran. 88 (2015) 42–54.

[34] M. V. Papalexandris, A two-phase model for compressible granular flows based on the theory of irreversible processes, J. Fluid Mech. 517 (2004) 103–112.

[35] D. W. Schwendeman, C. W. Wahle, A. K. Kapila, The Riemann problem and a high-resolution godunov method for a model of compressible two-phase flow, J. Comput. Phys. 212 (2006) 490–526.

[36] V. Deledicque, M. V. Papalexandris, An exact Riemann solver for compressible two-phase flow models containing non-conservative products, J. Comput. Phys. 222 (2007) 217–245.

[37] M. Dumbser, D. S. Balsara, A new efficient formulation of the HLLEM Riemann solver for general conservative and non-conservative hyperbolic systems, J. Comput. Phys. 304 (2016) 275–319.

[38] M. Short, J. W. Dold, Linear stability of a detonation wave with a model three-step chain-branching reaction, Math. Comput. Model. 24 (1996) 115–123.

[39] M. Short, J. J. Quirk, On the nonlinear stability and detonability limit of a detonation wave for a model three-step chain-branching reaction, J. Fluid Mech. 339 (1997) 89—-119.

[40] G. J. Sharpe, N. Maflahi, Homogeneous explosion and shock initiation for a three-step chain-branching reaction model, J. Fluid Mech. 566 (2006) 163—-194.

[41] D. Stewart, A. R. Kasimov, State of detonation stability theory and its application to propulsion, J. Propul. Power 22 (2006) 1230.

[42] J. B. Bdzil, D. S. Stewart, The dynamics of detonation in explosive systems, Ann. Rev. Fluid Mech. 39 (207) 263–292.

[43] Z. Wang, C. K. Law, An analysis of the explosion limits of hydrogen-oxygen mixtures, J. Chem. Phys 138 (2013) 134305.

[44] M. V. Papalexandris, Combustion and Fuels, Presses Universitaires de Louvain, 2020.

[45] M. V. Papalexandris, A. Leonard, P. Dimotakis, Unsplit schemes for hyperbolic conservation laws with source terms in one space dimension, J. Comput. Phys. 134 (1997) 31–61.

[46] M. V. Papalexandris, A. Leonard, P. Dimotakis, Unsplit algorithms for multidimensional hyperbolic systems of conservation laws with source terms, Comput. Math. Appl. 44 (2002) 25–49.

[47] F. Sonnenwald, V. Stovin, I. Guymer, Estimating drag coefficient for arrays of rigid cylinders representing emergent vegetation, J. Hydraul. Res. 57 (4) (2019) 591–597.

[48] F. P. Incropera, D. P. DeWitt, T. L. Bergman, A. Lavine, Fundamentals of heat and mass transfer, 6th edition, John Wiley, 2007.

[49] M. V. Papalexandris, Numerical simulation of detonations in mixtures of gases and solid particles, J. Fluid Mech. 507 (2004) 94–142.

[50] M. V. Papalexandris, Influence of inert particles on the propagation of multidimensional detonation waves, Combust. Flame 141 (2005) 216–228.

[51] C. Johansen, G.Ciccarelli, Combustion in a horizontal channel partially filled with a porous media, Shock Waves 18 (2008) 97–106.

[52] P. D. Antoniadis, M. V. Papalexandris, Dynamics of shear layers at the interface of a highly porous medium and a pure fluid, Phys. Fluids 27 (2015) 014104.